Exploring aluminium ion insertion into magnesium doped manjiroite (MnO₂) nanorods in aqueous solution

Jickson Joseph, [a]# Joseph F. S. Fernando, [a,b]# Md Abu Sayeed, [a,b] Cheng Tang, [a,b] Dmitri Golberg, [a,b] Aijun Du, [a,b] Kostya (Ken) Ostrikov, [a,b] and Anthony P. O'Mullane* [a,b]

[a]   Dr. J. Joseph, Dr. J. F. S. Fernando, Dr. Md A., Sayeed, Mr. C. Tang, Prof. D. Golberg, Prof. A. Du, Prof. K. Ostrikov, Prof. A. P. O'Mullane
        School of Chemistry and Physics, Queensland University of Technology (QUT), Brisbane, QLD 4000, Australia
        E-mail: anthony.omullane@qut.edu.au
[b]   Dr. J. F. S. Fernando, Dr. Md A., Sayeed, Mr. C. Tang, Prof. D. Golberg, Prof. A. Du, Prof. K. Ostrikov, Prof. A. P. O'Mullane
        Centre for Materials Science, Queensland University of Technology (QUT), Brisbane, QLD 4000, Australia.
        # equal contribution
        Supporting information for this article is given via a link at the end of the document.

Abstract: Aqueous aluminium ion batteries are promising for sustainable energy storage given the abundance of aluminium and their ease of recycling. However, finding suitable electrode materials that can intercalate Al-ions remains challenging. Here we investigate Mg ion doped MnO₂ nanorods in the manjiroite structure that allow Al-ion insertion into the open tunnels of this material. The electrode material has been characterized before and after Al-ion insertion with X-ray diffraction and X-ray photoelectron spectroscopy as well as studying the insertion process via *in situ* transmission electron microscopy which highlighted a change in the length of the MnO₂ nanorod. The results indicate that Al-ions can be successfully inserted into the MnO₂ nanorods which was determined by density functional theory calculations to be an energetically favourable process. The electrochemical data indicates that diffusion-controlled Al insertion as well as a surface pseudocapacitive effect occur. This indicates that MnO₂ nanomaterials synthesised in the presence of metal cations is potentially a viable route for facilitating their use as electrode materials in aqueous Al ion batteries or supercapatteries.

Introduction

The growing demand for clean renewable energy has resulted in an urgent requirement for efficient energy storage technologies. To fully harness the benefits of intermittent renewable energy sources such as wind and solar the excess electricity generation needs to be stored efficiently. Several technologies are available for this, namely chemical storage in the form of hydrogen or hydrogen carriers and batteries. For the latter, large scale battery storage has been demonstrated by numerous pilot studies as well as commercially viable installations.[1] To date Li ion batteries have dominated the sector but there are significant efforts in undertaking new approaches and developing new technologies such as organic and inorganic redox flow batteries[2-3] and going beyond traditional Li ion batteries such as potassium and sodium ion batteries[4-5] and multivalent ion batteries based on Zn, Mg, Ca, Fe and in particular Al.[6-13] The use of multivalent ion batteries is attractive because the multivalent ions in the electrolyte can transport more electrons per cation with a comparable amount of ion storage compared to Li ions.[14]

Al ion batteries in particular have been identified as a promising new technology due to the numerous potential benefits of employing Al ions and/or Al metal as the anode material such as having a large theoretical volumetric capacity of 8046 mAh/ml, low cost and natural abundance.[15] If aqueous Al ion batteries (AAIBs) are considered then additional benefits include environmental and operational safety which is a concern when organic electrolytes are used. In addition, aqueous batteries will be easier to recycle at their end of life which is also becoming a pressing issue with current battery technology which largely ends up in landfill.[16] Although these advantages are considerable there are still relatively few studies on AAIBs. This is largely because electrode materials that facilitate aluminium ion intercalation have not been extensively identified and tested for the production of a high performance battery.[17-18] Liu *et al* initially reported a half-cell using TiO₂ nanotube arrays and an AlCl₃ electrolyte.[17] The same group also reported a full AAIB cell with a copper hexacyanoferrate cathode using an Al₂(SO₄)₃ electrolyte.[19] Recently MnO₂ has been proposed as a cathode material with aluminum metal as the anode which was modified with an ionic liquid to make a full aqueous AAIB.[20] Other examples of electrode materials suitable for Al ion batteries include spinel MnO₂[21] TiO₂,[22-23] copper hexacyanoferrate (CuHCF)[19] and V₂O₅.[24] Zhou *et al* has shown that a Prussian blue analogue type FeFe(CN)₆ cathode is appropriate when using a water in salt electrolyte of 5 M Al(CF₃SO₃)₃.[25] It has also been reported that flexible AAIBs are possible using a CuHCF cathode and polypyrrole coated MoO₃ anode sandwiched by a gel electrolyte.[14] Recently our group has been exploring other potential electrode materials including MoO₃[26] and potassium rich cryptomelane[27] as candidates for use in AAIBs.

In this work we investigate Mg doped MnO₂ nanorods, which is based on an Earth abundant MnO₂ phase for its suitability as a candidate electrode material for Al-ion intercalation. It is found that synthesising MnO₂ in the presence of Mg²⁺ ions creates the manjiroite structure which provides ion intercalation sites for Al³⁺ ions in the tunnels of the material as supported by density functional theory calculations. This approach to creating open structured metal oxides using metal cations which allows for enhanced Al ion intercalation is outlined for the current system in Scheme 1 and may also be applicable to other multivalent ion systems.
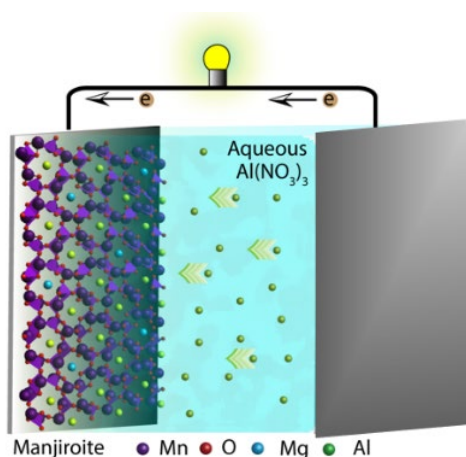
Scheme 1. Illustration showing the intercalation of Al^{3+} ions into the tunnel structure of manjiroite Mg-MnO_2.

Results and Discussions

In this work we synthesised Mg doped MnO_2 (Mg-MnO_2) nanorods (manjiroite structure) with tetragonal crystal structures through a simple hydrothermal method. An X-ray diffraction (XRD) pattern of this material is shown in Figure S1 which confirms its crystalline structure where the peaks match the standard pattern of the pure tetragonal manjiroite phase (PDF card file 01- 085-4054) which belongs to the cryptomelane mineral group with tetragonal I4/m space group (a = 9.916 Å, c = 2.864Å).[28] This crystallographic data matches well with that of MnO_2 obtained from the oxidation zone of metamorphosed manganese deposits.[29] Therefore in principle such manganese ores could be used directly as cathode materials without any further modification. The crystal structure is built of MnO_6 octahedra that form tunnels with a pore size of 4.6 Å or even larger depending on the doped metal in the tunnel where these ions can in principle be exchanged with solution ions when a potential is applied to the host material. In this example using Al^{3+} ions in solution the intercalation/deintercalation space for Al ion insertion is generated due to the presence of Mg^{2+} ions (0.72 Å)[30] which have a larger ionic radius compared to Al^{3+} ions (0.51 Å). Although the hydrated radii of Al^{3+} will be higher than Mg^{2+} in aqueous electrolyte, it has been demonstrated previously that the hydrated shell around the solution phase ion will be removed at the electrode interface and that the non-hydrated ions are intercalated into the MnO_2 lattice structure as demonstrated when using Mg^{2+} ions.[31]

Scanning electron microscopy (SEM) and transmission electron microscopy (TEM) were employed to obtain a thorough morphological and structural assessment of the manjiroite MnO_2 nanorods. SEM images (Figure 1a) confirm the uniform distribution of the nanorod morphology over broad domains in the prepared samples. The TEM image in Figure 1b shows that the as-prepared MnO_2 consists of uniform, 30 to 50 nm diameter nanorods. This distinctive architecture should in principle improve electrical activity because of the large surface area, resulting in an excellent electrode / electrolyte interface and a small ion diffusion route. The selected area electron diffraction (SAED) pattern in Figure 1b also indicates the highly crystalline nature of the sample, where diffraction spots corresponding to

the {200}, {130} and {211} planes of the manjiroite structure were clearly identified. The high-resolution TEM image (Figure 1c) shows the crystal orientation and structure and demonstrates that the *d* spacing of these obtained fringes is 0.70 nm, which corresponds to an interplanar distance of {110} planes of the manjiroite structure.[32] The dark field scanning transmission electron microscopy (DF-STEM) image and energy dispersive spatially resolved X-ray (EDX) maps confirm the uniform distribution of manganese and oxygen in the nanorods
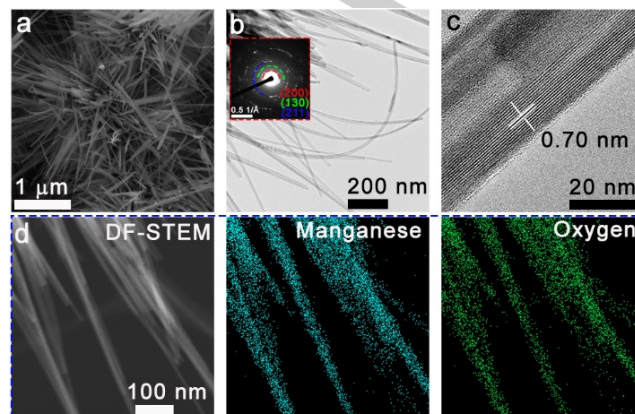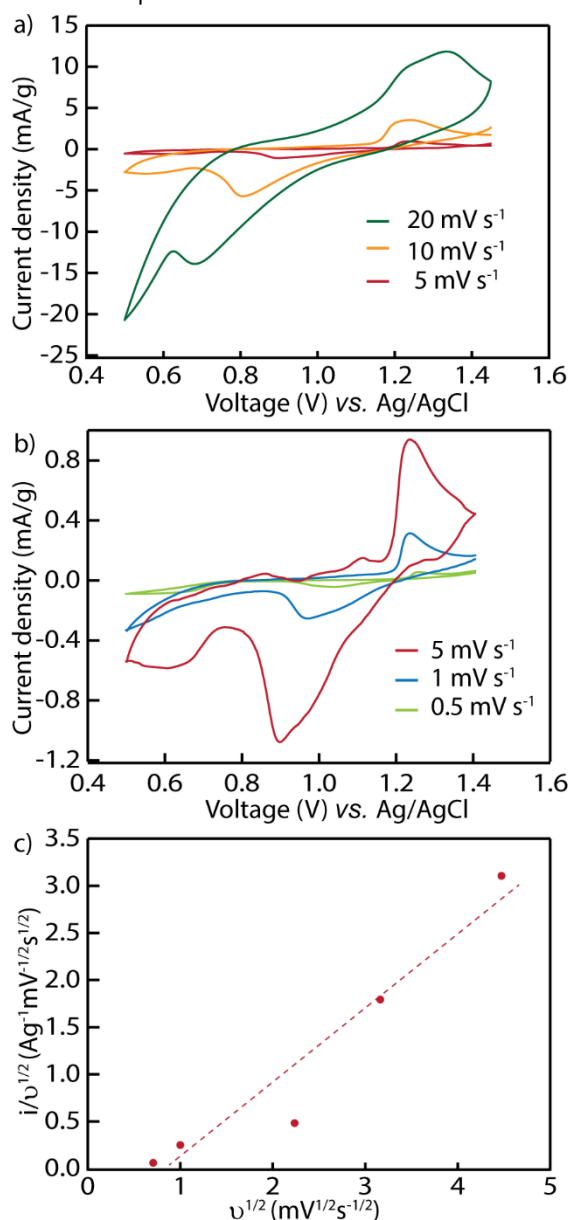

(Figure 1d).

Figure 1. (a) SEM image of manjiroite MnO_2 nanorods which shows their uniform distribution. (b) TEM image with SAED pattern, (c) high resolution TEM image of the nanorods showing the lattice fringes and (d) DF-STEM image and the corresponding EDX maps.

Cyclic voltammograms (CVs) of the obtained manjiroite MnO_2 nanorods in an aqueous $Al(NO_3)_3$ solution were measured and are displayed in Figure 2a to verify the feasibility of reversible Al^{3+} ion insertion/extraction. A quasi-reversible process is identified with redox peaks at 0.8 and 1.2 V (vs. Ag/AgCl at 5 mV s^{-1}) corresponding to the insertion and extraction of Al^{3+} ions into and out of MnO_2, respectively. This broad response is similar to previous work which demonstrated the insertion/extraction of Mg^{2+} ions at λ-MnO_2,[33] and Zn^{2+} ions at δ-MnO_2.[34] The hydrogen evolution reaction was observed in the cathodic scan after Al^{3+} ion insertion at a potential of 0.1 V (vs. Ag / AgCl), indicating that Al^{3+} ion insertion is preferred over the reported potential range in Figure 2a. It was also found that Mg ion doping was required to observe such a redox response as the control undoped MnO_2 sample did not show any evidence of a quasi-reversible redox process over the same potential range (Figure S2). This indicates that the Mg ions occupying the tunnels in this phase of MnO_2 are required for the insertion of Al^{3+} ions from solution as confirmed below via spectroscopic experiments. This is consistent with our previous work with K^+ rich cryptomelane MnO_2 which resulted in the exchange of K^+ ions with Al^{3+} ions.[27]

At the faster sweep rates of 10 and 20 mV s^{-1} there is only one peak visible, however at lower sweep rates (1 and 5 mV s^{-1}) the main cathodic process begins to resolve into two processes where a shoulder becomes visible prior to the main peak. This indicates that Mn^{4+} may be reduced to both Mn^{3+} and Mn^{2+} during the reduction process where the charge is compensated via the insertion of Al^{3+} ions. On the anodic sweep there is also evidence of peak splitting when the electrode is oxidised. It should be noted that at higher sweep rates the anodic and

cathodic peaks were still observed and not a rectangular shaped process which suggests that this process is not only capacitive but contains a diffusion-controlled contribution to the current. For this type of system the peak current can be related to the sweep rate of the experiment via the following equation: $I = k_1 v + k_2 v^{0.5}$, where k_1 and k_2 are constants.[35] The first term corresponds to surface mediated ion storage (or capacitive) behaviour while the second term is attributed to a diffusion-controlled ion insertion process. It was found for this system that there is a linear dependence of $I/v^{0.5}$ versus $v^{0.5}$ which indicates contributions from both capacitive and diffusion-controlled processes (Figure 2c).[36] Therefore, the manjiroite MnO_2 nanorods act as a pseudocapacitive material which is controlled by a surface as well as diffusion process.


Figure 2. Cyclic voltammograms of Mg-MnO_2 nanorods in 1 M Al(NO₃)₃ electrolyte recorded at different sweep rates (a-b) and (c) a plot of $I/v^{0.5}$ versus $v^{0.5}$ form the data in parts a and b.

There is also the possibility that the redox responses are due to proton insertion/extraction which is encountered for transition

metal oxide materials.[37] Therefore to investigate this effect cyclic voltammetry experiments were performed in 1 M HNO_3 which did not exhibit any well-defined quasi-reversible reduction/oxidation processes (Figure S3). This indicates that the peaks observed in Figure 2 are due to the reduction of MnO_2 where the change in oxidation state is compensated by Al-ion insertion.

In order to confirm the hypothesis that Al^{3+} ion insertion occurs in the nanorods and not confined purely to the surface, which would indicate a purely capacitive process, XRD patterns of the pristine and Al-ion inserted electrode were measured (Figure 3). It can be observed that the electrode maintains its crystal structure upon Al-ion insertion as the peaks are consistent between the two samples (Figure 3a). Rietveld refinement showed that both electrodes could be indexed to the manjiroite structure (Figure S4), indicating that no significant structural change occurs upon Al ion insertion. However, upon closer inspection of the peaks, it was observed that there were slight shifts in the peak positions to higher values of 2θ (Figure 3b). When the XRD patterns were analysed and Pawley fitting performed it was found that the lattice parameters changed after Al ion insertion. For the pristine electrode, a = 9.950(3) Å and c = 2.801(9) Å while for the reduced electrode a = 9.886(3) Å and c = 2.8576(2) Å. This indicates that the nanorod crystal becomes elongated with a slight contraction in the width once Al ions are inserted into the structure. When the Al ions were extracted from the sample it was observed from the XRD pattern (Figure 2c) that the peaks stayed in the same position indicating that the nanorods to do not contract upon removal of the Al ions.
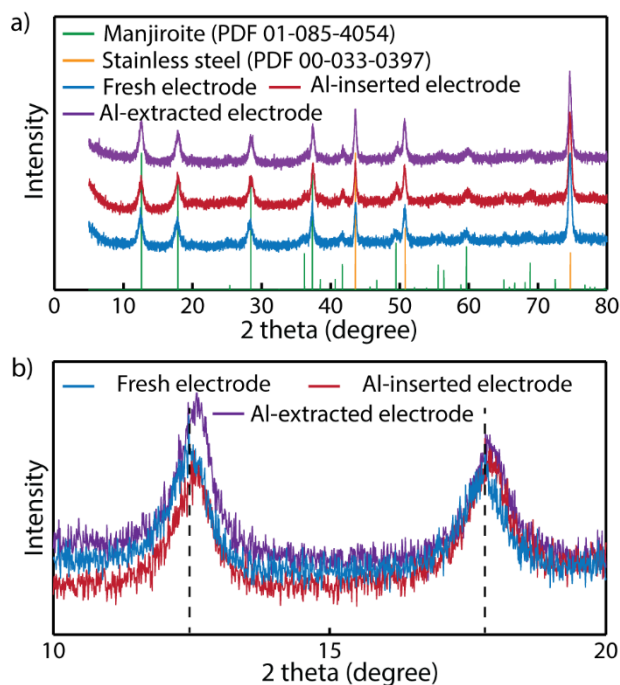
Figure 3. a) Comparison of XRD patterns of fresh, reduced and oxidised samples on a stainless steel current collector electrode where b) shows an enlarged part of the obtained XRD patterns.

In addition, X-ray photoelectron spectroscopy (XPS) measurements were also used to examine the reaction mechanism further and to verify whether Al-ions are intercalated

into the manjiroite lattice during the reduction process. The samples were etched for 120 s prior to the test to prevent any possible contributions from Al^{3+} ions on the surface and any surface contamination that could have occurred after washing the electrodes post cycling. Figure 4 shows XPS spectra of the fresh and reduced electrodes made of manjiroite $Mg-MnO_2$ nanorods. The survey spectrum in Figure S5 also shows the presence of peaks at 686.8 eV and 284.8 which can be attributed to F 1s and C 1s, that are due to the presence of the PVDF binder and activated carbon. Upon Al ion insertion there is the appearance of an Al peak in the survey spectrum. These changes can be seen more clearly in the high-resolution spectra
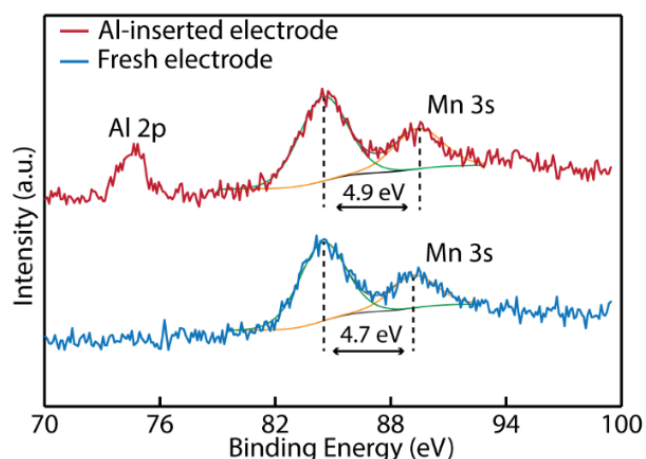

(Figure 4). Initially the Mn 2p spectrum was investigated (Figure S5) where peaks at 653.7 and 641.9 eV are assigned to the Mn $2p_{1/2}$ and $2p_{3/2}$ core levels. After insertion of Al there was no distinctive change in the

Figure 4. XPS Mn 3s spectra of fresh and Al inserted electrode which also shows the Al 2p region.

XPS spectrum as is often the case for Mn 2p spectra where assignment of oxidation states is unreliable. Therefore, we investigated the Mn 3s spectrum to observe any changes in the oxidation state (Figure 4). Here, the multiplet peaks result from the exchange interaction between the core level electron (3s) and the unpaired electrons in the valence band level (3d) by photoelectron ejection.[38] The multiplet splitting of Mn 3s peaks can be used for determining the oxidation state of Mn[39] where in this case the splitting energy of the fresh and reduced electrodes are 4.73 eV and 4.93 eV, respectively which indicates a reduction in the oxidation state of the MnO_2 material. This difference of 0.2 eV is consistent with previous reports on

electrodeposited MnO_2 films where the deposition method influenced the final oxidation state of the material.[40] This data is tabulated in Table S1. It can also be observed that the Al 2p peak is present in this binding energy range. For the fresh electrode there is an absence of Al, however after Al insertion the presence of Al is evident at 74 eV which can be attributed to Al^{3+}.[41]

An *in-situ* TEM analysis was performed to study the Al^{3+} insertion behaviour and the structural stability of $Mg-MnO_2$ nanorods. Figure 5a shows a photograph and a schematic illustration of the *in-situ* TEM setup. $Al(NO_3)_3$ salt was loaded on a piezo-driven tungsten wire, whereas the prepared nanorod sample was placed on the stationary gold wire. This setup is not a full representation of the Al ion battery, however, can be implemented to study how the nanorod sample behaves upon Al^{3+} insertion. Figure S6 shows a low magnification TEM image of the nanorod sample selected for the *in-situ* TEM experiment. These two electrodes were then brought into contact in the microscope and the process was continuously imaged (Movie S1). There was no notable change to the $Mg-MnO_2$ nanorod upon initial contact with $Al(NO_3)_3$. Then a - 2 V (*vs* counter electrode $W/Al(NO_3)_3$ was applied to initiate the Al^{3+} insertion into the $Mg-MnO_2$ nanorod. Interestingly, a minor elongation of the $Mg-MnO_2$ nanorod was observed (Movie S2). The length of the nanowire was monitored between two points as shown in Figure 5b to 5d (the length of the blue arrow is kept constant to perceive the elongation of nanorod). It was observed that length between these two points increased from 530 nm to 563 nm in ~ 120 seconds. This minor elongation (~ 6.2%) in fact indicates ready uptake of Al^{3+} by the nanorod sample without major changes to the structure or morphology. Figure 5e displays the voltage and current transients across the nanorod during Al^{3+} insertion process. Upon applying a bias of - 2V, the current through the nanorod sharply increased to - 2 nA, and then gradually increased to ~ - 4 nA over 120 seconds. This observation indicates Al^{3+} insertion and good conductivity of the $Mg-MnO_2$ nanorod sample. An EDX line scan was performed (as marked in Figure 5d) to further confirm the insertion of Al^{3+} into the $Mg-MnO_2$ nanorod (refer supporting information for DF-STEM image acquired for the line scan and additional details, Figure S7). The presence of Al within the nanorod is evident as displayed in the EDX line scan profiles in Figure 5f and 5g. Notably the counts for Mg is relatively low compared to that of Al. Figure 5h shows the EDX spectrum (1.0 – 3.0 keV region) corresponding to the line scan profiles, where the peak at 1.487 keV is attributed to Al Kα radiation further confirming the insertion of Al^{3+}.
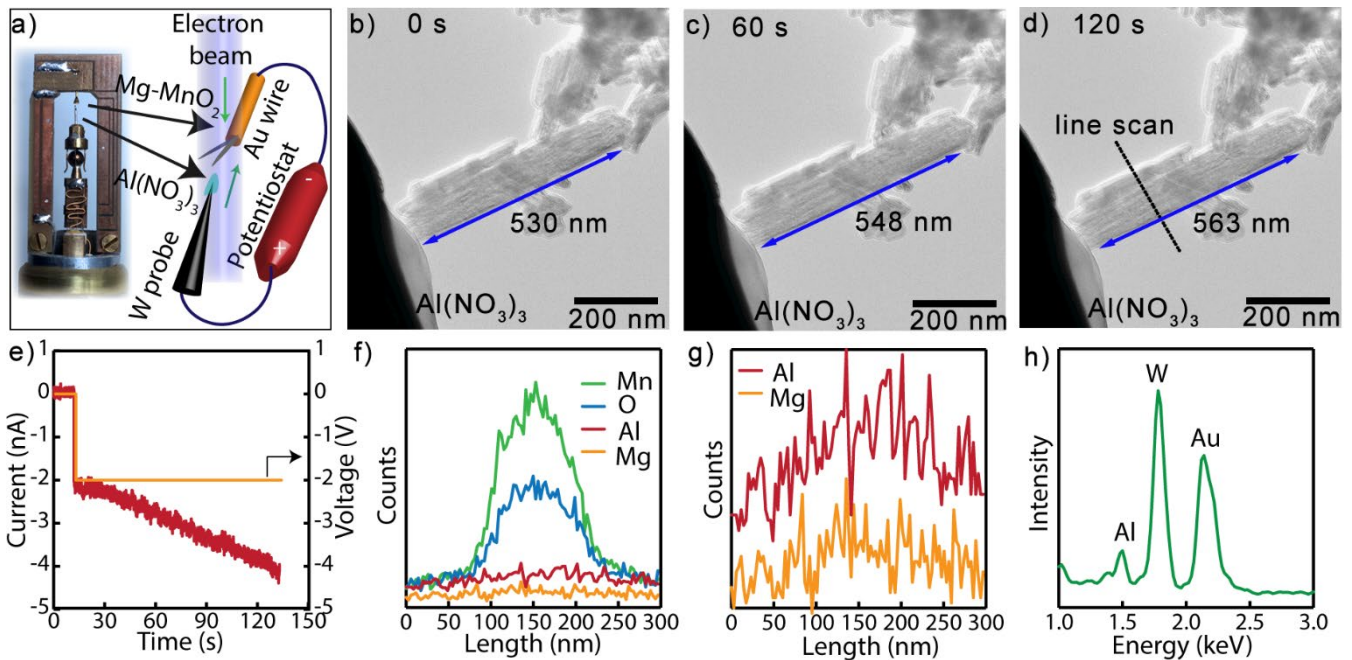
Figure 5. a) Photograph and schematic illustration of the *in situ* TEM setup. b) TEM image acquired before applying a bias of -2 V. c) and d) Time dependent TEM images acquired at 60 s and 120 s, respectively, when applying a bias of -2 V. e) Voltage and current transients during Al^{3+} insertion. f) STEM-EDX line scan profiles obtained from the line marked in 5d. g) Line scan profile showing Al and Mg only. h) EDX spectrum corresponding to the line scan profile (1.0 – 3.0 keV region).

In order to understand the effect on Al^{3+} intercalation, we calculated the formation energy (E_f) of Al^{3+} intercalated Mg-MnO_2, which is defined as:

$$E_f = E_{xAl-MnO_2} - E_{Mg-MnO_2} + x\mu_{Mg} - x\mu_{Al} ,$$

where $E_{xAl-MnO_2}$ and E_{Mg-MnO_2} are total energies of the MnO_2 structure with and without Al^{3+} intercalation, while x represent the number of the intercalated Al^{3+}. μ_{Mg} and μ_{Al} are the chemical potential of Mg^{2+} and Al^{3+} ions, which are calculated by setting single atom in a cubic crystal with the parameter a = 10 Å. As shown in Figure 6, for single Al^{3+} intercalation, the calculated energy reaches -2.90 eV, indicating its thermal stability. Compared with the formation energy of single Al^{3+} intercalated Mg-MnO_2 (-2.49 eV), the more negative value suggests that Al^{3+} ions are more likely to substitute Mg^{2+} ones. Besides, we also examined the formation energy of the Al^{3+} completely

intercalated case. The formation energy of -9.37 eV indicates that the following Al^{3+} intercalation is also energetically favorable. Therefore, Al^{3+} intercalated MnO_2 is much more stable than Mg^{2+} one, suggesting the promising application in Al^{3+} ion storage.

Figure 6. The optimized 2×2×1 supercells for (a) Mg rich, (b) single Al^{3+} intercalated, and (c) Al^{3+} completely intercalated structure. Purple, red, orange and light blue spheres represent Mn, O, Mg and Al atoms.

Conclusion

In summary, we have demonstrated the feasibility of an electrochemical aluminum insertion reaction of Mg-doped manjiroite MnO_2 nanorods prepared by a simple hydrothermal synthesis method in a 1 M $Al(NO_3)_3$ aqueous electrolyte. It was found that the open structure of the manjiroite nanorods, synthesised in the presence of Mg^{2+} ions, thereby creating tunnel vacancies was the key aspect for the insertion / de-intercalation of Al^{3+} ions. In addition, there is a surface mediated ion storage process which also contributes to this electrode acting as a pseudocapactive material. This work offers an insight into the development of intercalation nanomaterials that contain guest species which may have potential use as electrode materials for aqueous rechargeable multi-valent ion batteries or supercapatteries.

Experimental Section

The materials were synthesized using an easy hydrothermal technique. 0.625 M $MgSO_4$ was mixed into 30 ml deionized water for the typical

1
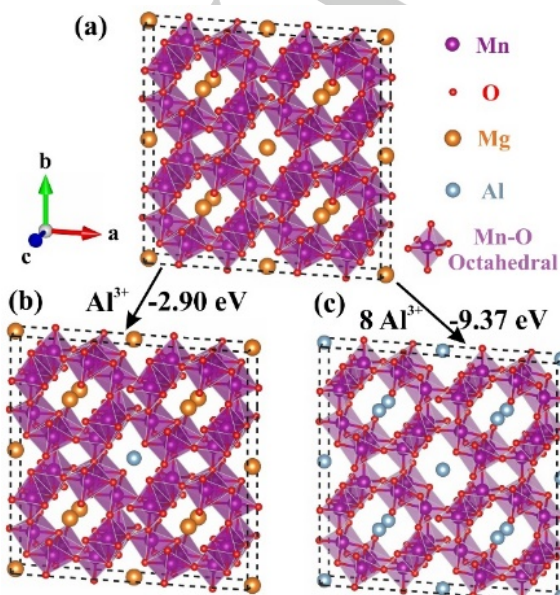
synthesis. After 10 min of stirring, 30 mL of 0.25M $MnSO_4$ and 0.25M $NH_4S_2O_8$ were added to the $MgSO_4$ solution, followed by 2 ml of H_2SO_4. The solution was kept for 60 min of stirring before transferring it into a 100 mL Teflon stainless steel autoclave and was heated at 120°C for 24 h and then allowed to cool to room temperature. The resulting black product was centrifugally recovered and washed several times with deionized water and ethanol and subsequently dried for 6 h at 70°C.

The Rigaku SmartLab diffractometer (Cu source, 40 kv 40 mA) in the Bragg-Brentano geometry with the Hypix 3000 detector was used for collection of Powder X-ray diffraction patterns. A divergent optical mirror (CBO-α) was used. Patterns of 3-80° 2θ for a step of 0.01° were collected for half an hour per sample. XPS data were collected using a Kratos AXIS Supra photoelectron spectrometer. SEM imaging was carried out using a JEOL 7001 microscope. TEM, STEM, SAED and EDX analysis was performed using a JEOL 2100 UHR microscope. "Zues" scanning tunnelling microscopy (STM)-TEM *in situ* specimen holder (Zeptools, P.R China) was used for the *in-situ* TEM work. All electrochemical experiments used a three-electrode configuration with the Biologic VSP3 potentiostat. Glassware were rinsed with reagent water of type I (EMD Millipore, resistivity of 18 M da cm). As a working electrode substrate, Stainless Steel (SS) (MTI Corp) was employed. SS slides were cut into 1 cm x 2 cm form and cleaned with acetone and dried at 60 C before they have been coated with electrode slurry. Manjiroite nanorods, PVDF, N-Methyl-2-pyrrolidone and activated carbon were mixed at a ratio of 8:1:1 to make the electrode slurry. This electrode slurry was stirred for 1 h to obtain homogenous mixing. This slurry was coated on stainless steel to make a thin film. These coated electrodes were maintained for 3 h at 140°C in vacuum atmosphere. 3-electrode studies were performed in 1 M $Al(NO_3)_3$ electrolytes with Ag / AgCl (BASi, filled with 3 M KCl) in and in graphite rod (rod, L 150 mm, diam. 3 mm and low density, 99,995 percent Sigma Aldrich base trace metals).

The first-principles calculations were performed at the level of Perdew-Burke-Ernzerhof (PBE) functional of generalized gradient approximation (GGA)[42] within projector-augmented wave (PAW) method[43], as implemented in Vienna *ab initio* simulation package (VASP)[44-45]. The kinetic cut-off energy was set to be 500 eV, and the k-points for first Brillouin zone were sampled by a Monkhorst k-mesh of 5×5×11. The geometric optimizations were terminated until the energy of each atoms converged to 10^{-6} eV and the force of them became less than 0.001 eV/Å. Besides, the effect on spin of Mn atoms was considered in our calculations, and a 2×2 supercell was adopted to reduce the concentration of Al^{3+} intercalated conditions. Note that the structures of Mg^{2+}-rich cryptomelane show large distortion during the full relaxation, due to the strong interactions between Mg and O atoms. Thus, we manually changed the crystal parameters in a large range with the step of 0.01 Å and fixed them during geometric optimization.

[1]   H. Poulter, in *Decentralised Energy: A Global Game Changer*, ed. C. Burger, Ubiquity Press, London, 2020.
[2]   S. Gentil, D. Reynard, H. H. Girault, *Curr. Opinion Electrochem.*, **2020**, *21*, 7-13.
[3]   R. Chen, *Curr. Opinion Electrochem.*, **2020**, *21*, 40-45.
[4]   W. Zhang, Y. Liu, Z. Guo, *Sci. Adv.*, **2019**, *5*, eaav7412.
[5]   M. Chen, Y. Zhang, G. Xing, Y. Tang, *Front. Chem.*, **2020**, *8*.
[6]   P. Canepa, G. Sai Gautam, D. C. Hannah, R. Malik, M. Liu, K. G. Gallagher, K. A. Persson, G. Ceder, *Chem. Rev.*, **2017**, *117*, 4287-4341.
[7]   G. A. Elia, K. V. Kravchyk, M. V. Kovalenko, J. Chacón, A. Holland, R. G. A. Wills, *J. Power Sources*, **2021**, *481*, 228870.
[8]   K. V. Kravchyk, C. Seno, M. V. Kovalenko, *ACS Energy Lett.*, **2020**, *5*, 545-549.
[9]   T. Leisegang, F. Meutzner, M. Zschornak, W. Münchgesang, R. Schmid, T. Nestler, R. A. Eremin, A. A. Kabanov, V. A. Blatov, D. C. Meyer, *Front. Chem.*, **2019**, *7*, 268.
[10]   D. Yuan, J. Zhao, W. Manalastas, S. Kumar, M. Srinivasan, *Nano Mater. Sci.*, **2020**, *2*, 248-263.
[11]   S. K. Das, S. Mahapatra, H. Lahan, *J. Mater. Chem. A*, **2017**, *5*, 6347-6367.
[12]   X. Li, Y. Tang, J. Zhu, H. Lv, L. Zhao, W. Wang, C. Zhi, H. Li, *Small*, **2020**, *16*, 2001935.
[13]   H. Li, L. Ma, C. Han, Z. Wang, Z. Liu, Z. Tang, C. Zhi, *Nano Energy*, **2019**, *62*, 550-587.
[14]   P. Wang, Z. Chen, Z. Ji, Y. Feng, J. Wang, J. Liu, M. Hu, H. Wang, W. Gan, Y. Huang, *Chem. Eng. J.*, **2019**, *373*, 580-586.
[15]   J. Muldoon, C. B. Bucur, T. Gregory, *Chem. Rev.*, **2014**, *114*, 11683-11720.
[16]   A. Mayyas, D. Steward, M. Mann, *Sustainable Mater. Technol.*, **2019**, *19*, e00087.
[17]   S. Liu, J. Hu, N. Yan, G. Pan, G. Li, X. Gao, *Energy Environ. Sci.*, **2012**, *5*, 9743-9746.
[18]   Y. Liu, S. Sang, Q. Wu, Z. Lu, K. Liu, H. Liu, *Electrochim. Acta*, **2014**, *143*, 340-346.
[19]   S. Liu, G. Pan, G. Li, X. Gao, *J. Mater. Chem. A*, **2015**, *3*, 959-962.
[20]   Q. Zhao, M. J. Zachman, W. I. Al Sadat, J. Zheng, L. F. Kourkoutis, L. Archer, *Sci. Adv.*, **2018**, *4*, eaau8131.
[21]   C. Wu, S. Gu, Q. Zhang, Y. Bai, M. Li, Y. Yuan, H. Wang, X. Liu, Y. Yuan, N. Zhu, *Nat. Commun.*, **2019**, *10*, 73.
[22]   M. Kazazi, P. Abdollahi, M. Mirzaei-Moghadam, *Solid State Ionics*, **2017**, *300*, 32-37.
[23]   Y. J. He, J. F. Peng, W. Chu, Y. Z. Li, D. G. Tong, *J. Mater. Chem. A*, **2014**, *2*, 1721-1731.
[24]   J. González, F. Nacimiento, M. Cabello, R. Alcántara, P. Lavela, J. Tirado, *RSC Adv.*, **2016**, *6*, 62157-62164.
[25]   A. Zhou, J. Jiang, J. Yue, Y. Tong, Q. Zhang, Z. Lin, B. Liu, C. Wu, L. Suo, Y.-S. Hu, H. Li, L. Chen, *ACS Appl. Mater. Interf.*, **2019**, *11*, 41356-41362.
[26]   J. Joseph, A. P. O'Mullane, K. Ostrikov, *ChemElectroChem*, **2019**, *6*, 6002-6008.
[27]   J. Joseph, J. Nerkar, C. Tang, A. Du, A. P. O'Mullane, K. Ostrikov, *ChemSusChem*, **2019**, *12*, 3753-3760.
[28]   C. Biagioni, C. Capalbo, M. Pasero, *Eur. J. Mineralogy*, **2012**, *25*, 85-90.
[29]   M. Nambu, K. Tanida, *J. Japanese Association of Mineralogists, Petrologists and Economic Geologists*, **1967**, *58*, 39-54.
[30]   H. Zhang, K. Ye, K. Zhu, R. Cang, X. Wang, G. Wang, D. Cao, *ACS Sustainable Chem. Eng.*, **2017**, *5*, 6727-6735.
[31]   J. Song, M. Noked, E. Gillette, J. Duay, G. Rubloff, S. B. Lee, *Phys. Chem. Chem. Phys.*, **2015**, *17*, 5256-5264.
[32]   M. Nambu, K. Tanida, *J. Mineralogical Soc. Japan*, **1980**, *14*, 62-85.
[33]   C. Yuan, Y. Zhang, Y. Pan, X. Liu, G. Wang, D. Cao, *Electrochim. Acta*, **2014**, *116*, 404-412.
[34]   S. Khamsanga, R. Pornprasertsuk, T. Yonezawa, A. A. Mohamad, S. Kheawhom, *Sci. Rep.*, **2019**, *9*, 8441.
[35]   J. Wang, J. Polleux, J. Lim, B. Dunn, *J. Phys. Chem. C*, **2007**, *111*, 14925-14931.

[36] H. Lahan, R. Boruah, A. Hazarika, S. K. Das, *J. Phys. Chem. C*, **2017**, *121*, 26241-26249.

[37] J. Z. Ou, S. Balendhran, M. R. Field, D. G. McCulloch, A. S. Zoolfakar, R. A. Rani, S. Zhuiykov, A. P. O'Mullane, K. Kalantar-zadeh, *Nanoscale*, **2012**, *4*, 5980-5988.

[38] M. Chigane, M. Ishikawa, *J. Electrochem. Soc.*, **2000**, *147*, 2246.

[39] V. Koleva, T. Boyadzhieva, E. Zhecheva, D. Nihtianova, S. Simova, G. Tyuliev, R. Stoyanova, *CrystEngComm*, **2013**, *15*, 9080-9089.

[40] F. Xiao, Y. Xu, *Int. J. Electrochem. Sci*, **2012**, *7*, 7440-7450.

[41] I. Milošev, T. Kosec, H.-H. Strehblow, *Electrochim. Acta*, **2008**, *53*, 3547-3558.

[42] J. P. Perdew, K. Burke, M. Ernzerhof, *Phys. Rev. Lett.*, **1996**, *77*, 3865.

[43] J. P. Perdew, S. Kurth, A. Zupan, P. Blaha, *Phys. Rev. Lett.*, **1999**, *82*, 2544.

[44] G. Kresse, J. Furthmüller, *Phys. Rev. B*, **1996**, *54*, 11169.

[45] G. Kresse, J. Furthmüller, *Computational Mater. Sci.*, **1996**, *6*, 15-50.

Entry for the Table of Contents
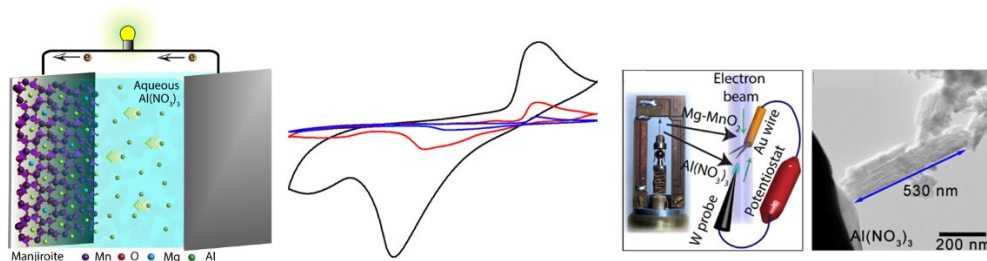
Mg ion doped MnO_2 nanorods facilitate Al ion insertion / extraction in a 1 M $Al(NO_3)_3$ electrolyte opening up their potential use as an electrode material for aqueous Al ion batteries.

Institute and/or researcher Twitter usernames: @AOMullane_echem